

# Vibrational strong coupling influences product selectivity in a model for post transition state bifurcation reactions

Subhadip Mondal,<sup>1</sup> Atul Kumar,<sup>1</sup> and Srihari Keshavamurthy<sup>1,\*</sup>

<sup>1</sup>*Department of Chemistry, Indian Institute of Technology, Kanpur, Uttar Pradesh 208 016, India*

(Dated: March 11, 2026)

Understanding the mechanism of chemical reaction rate modulation by vibrational strong coupling (VSC) has been the focus of several recent studies. However, a definitive explanation for the mode-specificity of VSC still eludes us. In this study, we highlight the dynamics under VSC by utilizing a model for post-transition state bifurcation (PTSB) reactions coupled to an optical cavity. The minimal two-dimensional PTSB model features a valley-ridge inflection (VRI) point leading to bifurcated energetically asymmetric product wells. Here, we are interested in exploring whether the product selectivity (branching ratios) in such PTSB systems, known to be sensitive to dynamical effects, can be significantly perturbed under VSC conditions. Detailed classical and quantum dynamical calculations, along with systematic variation of the model parameters, reveals that the branching ratio can be enhanced under VSC by nearly a factor of two. Interestingly, for certain parameter regimes we find excellent classical-quantum correspondence. Apart from emphasizing the role of both cavity-system and intramolecular energy transfer in the observed enhancements, our study brings out the complexity of VSC in terms of the choice of the cavity frequency vis-à-vis the various molecular mode frequencies. In addition, our work highlights the potential of cavity quantum electrodynamics as a tool for reshaping dynamical outcomes in reactions with complex potential energy landscapes.

## INTRODUCTION

The ability to steer chemical reactions by exciting specific molecular vibrational modes has been a long-standing goal for chemists. While the advent of lasers offered a potential pathway to this mode-specific chemistry, the phenomenon of intramolecular vibrational energy redistribution (IVR)[1–3], wherein excited modes resonantly couple with other vibrations and scramble the energy throughout the molecule, is thought to be a significant impediment. Therefore, in order to restore mode-specificity, one possibility, apart from overcoming the IVR timescale[4, 5], is to actively interfere with the IVR pathways. Indeed, aided to a large extent by the significant progress in our mechanistic understanding of IVR[6–8], recent studies show that it is possible to alter the IVR pathways by using external electric fields[9] as well as suitable chemical substitutions[10–13]. A clear indication from these studies is that tweaking the IVR pathways requires perturbing the network of anharmonic resonances that couple the various vibrational modes. In addition, we note that the relevance of IVR towards observing mode specificity in gas phase bimolecular reactions[14] has also been emphasized in recent years.

Lately, another approach towards achieving the “holy grail” of mode-specific chemistry has led to considerable enthusiasm. In this method, referred to as vibrational strong coupling (VSC), molecules are placed inside an optical cavity, and the cavity mode is tuned to resonance with a specific molecular vibration of interest[15–21]. The resulting formation of the hybrid light-matter

states (polaritons) has been shown to have a significant impact on rates and mechanisms of various reactions even in the absence of external light. Apart from reaction rate modulation, the influence of VSC has been investigated in a wide variety of systems. Recent examples include enhancement of electrical conductance in nonconducting polymers[22], quantum sensing[23, 24], modification of glass transition temperature of polymer films[25], and fabrication of nanoantennas[26]. Interestingly, there has been a suggestion to control IVR itself by utilizing an infrared photonic cavity[27]. At the same time, it is important to mention that there have been “null” experiments[28–30] which challenge our current understanding of the VSC mechanism. Consequently, there is an ongoing discussion regarding identifying polaritonic effects that are genuinely quantum[31–33] and beyond the optical filtering regime[34].

From a time-dependent point of view, the formation of polaritons implies energy exchange on the Rabi timescale between the cavity and the molecular mode. A natural question then is whether the cavity-molecule energy transfer, in the strong coupling limit, can significantly perturb the IVR pathways in the molecular system. Also, given that the specific IVR pathways that would be perturbed will depend on the vibrational mode that is involved in VSC, one may conjecture that this can lead to mode-specific effects. Although, there has been progress in this direction, a clear understanding of the potential competition between IVR and cavity-molecule energy exchange leading to mode-specific reaction dynamics is still lacking. Nevertheless, several studies[35–48] have contributed substantially towards gaining insights into the mechanism of VSC in terms of the crucial role played by the cavity-orchestrated molecular energy transfer process.

---

\* srihari@iitk.ac.in

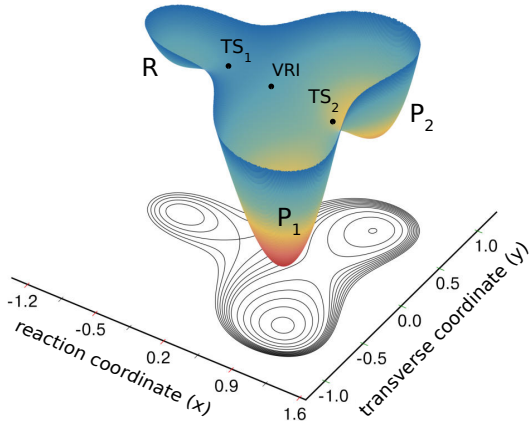


FIG. 1. Model potential energy surface Eq. 3 exhibiting a post transition state bifurcation. The reactant (R), transition states ( $TS_1$ ,  $TS_2$ ), products ( $P_1$ ,  $P_2$ ), and the valley ridge inflection (VRI) point are indicated.

Most of the theoretical studies mentioned above have employed models where one is dealing with a single reactant and single product scenario. Although this is a standard and useful model in the context of investigating VSC effects on reaction rates, multidimensional potential energy surfaces (PES) can harbor features like bifurcating reaction paths, higher rank saddles, and shallow intermediate states[49, 50]. Such features invariably lead to the existence of competing mechanisms and nonstatistical reaction dynamics. The current study is concerned with one such feature wherein reactions exhibit a post transition state bifurcation (PTSB)[51] due to the presence of a valley ridge inflection point on the PES. Essentially, as shown in Fig. 1, PTSB involves a single entrance transition state (also called “ambimodal”) bifurcating into two possible products without traversing through any intermediate states. Recently, reactions exhibiting PTSB have attracted considerable attention[52–55] due to that fact that in such systems dynamical effects[56, 57] and the shape of the PES[58], instead of the transition state energetics, control the product selectivity. It is important to note that one-dimensional model systems cannot mimic the PTSB feature, and hence a minimal model PES would require two degrees of freedom. The low dimensional PTSB model surface Fig. 1 utilized in this work already has several critical points (three minima and two transition states). Therefore, there are a multitude of frequencies to which the cavity mode can be tuned in order to explore the influence of VSC on selectivity. Consequently, our system of choice, although still lacking effects of dissipation and collective limit, presents a level of complexity that is absent in other model theoretical studies to date.

Here, we show that VSC does influence the product selectivity in the model system with clear indications

that the cavity-free dynamical effects can be amplified in the strong coupling regime. We find that VSC with the fundamental transition of the reactant well has minimal effect on the selectivity, whereas VSC involving the product wells leads to substantial influence on the selectivity. This observation resonates with the findings in a recent study by Ke[59] wherein maximal rate enhancement was observed at a cavity frequency corresponding to the product well transition, and different from the peak of the molecular absorption spectrum. Furthermore, as a surprising result in this context, we find that altering the depth of the product wells leads to a shift in the cavity frequency at which the maximum effect on the selectivity is observed. The mechanism involves a combination of factors involving cavity-system resonant energy exchange and interwell transitions leading to a cavity-mediated coherent cooling into both the product wells. The differing extent of cooling in the two product wells gives rise to the modulation of the branching ratio. Interestingly, we observe very good classical-quantum correspondence despite the absence of dissipation and cavity loss.

## THEORETICAL PRELIMINARIES

### Model Hamiltonian

The model Hamiltonian studied here, in the Coulomb gauge with the dipole approximation, has the Pauli-Fierz form and can be expressed as

$$H(\mathbf{r}, \mathbf{p}, q_c, p_c) = H_M(\mathbf{r}, \mathbf{p}) + \frac{1}{2}p_c^2 + \frac{1}{2}\omega_c^2 \left[ q_c + \frac{\lambda_c}{\omega_c} \mu(\mathbf{r}) \right]^2 \quad (1)$$

where  $\mathbf{r} \equiv (x, y)$  and  $\mathbf{p} \equiv (p_x, p_y)$  correspond to the matter coordinates and their conjugate momenta, respectively. The photon coordinate and momentum ( $q_c, p_c$ ) are associated with a single-mode cavity field of frequency  $\omega_c$ . The cavity field and matter are coupled via the dipole  $\mu(\mathbf{r})$  with strength  $\lambda_c$ , and note that the form of the interaction used includes the dipole self-energy term. We have taken the dipole to be aligned with the field polarization, as is typically assumed in such model studies. The matter Hamiltonian is given by

$$H_M(\mathbf{r}, \mathbf{p}) = \frac{1}{2m}(p_x^2 + p_y^2) + U(\mathbf{r}) \quad (2)$$

with  $m$  being the mass and the two-dimensional potential energy surface (PES)[58, 60]

$$U(\mathbf{r}) = \bar{V}^\dagger [Ax^4 - Bx_s x^3 - Cx_s^2 x^2] + Dy^2 + Fy^4 \quad (3a)$$

$$+ Gx^2 y^2 + Hxy^2(y^2 - 2) + \alpha xy \quad (3b)$$

models reactions which exhibit post transition-state bifurcation (PTSB). The form of the PES is shown in Fig. 1 where the reactant (R), products ( $P_1$ ,  $P_2$ ), and the two transition states ( $TS_1$ ,  $TS_2$ ) are indicated.

The PES depends on several parameters that determine the overall shape of the PES and the locations of the various critical points. The parameter  $V^\ddagger$  determines the reactant well depth relative to  $\text{TS}_1$  and the relative depths of the product wells. The parameter  $x_s$  sets the distance between R and  $\text{TS}_2$  while the parameters  $(\alpha, G, H)$  tune the coupling between the molecular modes. In particular,  $\alpha$  controls the extent of energetic asymmetry of the two product wells with  $\alpha = 0$  corresponding to the symmetric case. We fix the parameter values (in a.u), adapted from previous works[57, 58], to be  $V^\ddagger = 3/1280$ ,  $x_s = 0.2$ ,  $A = G = 1/2$ ,  $B = 2/3$ ,  $C = 12$ ,  $D = F = 2/5$ ,  $H = 1$ ,  $\alpha = 0.1$ , and mass  $m = 22034$  (mass of carbon atom). The choice for the value of the mass ensures that, given the values of the rest of the PES parameters, the various vibrational mode frequencies are in the mid-IR range (see Fig. 2a). Moreover, in typical reactions[53, 61] exhibiting PTSB, the key collective motions involve heavy atom vibrations and hence the effective mass is expected to be large. Further details about the location, energies, and stability of the critical points are provided in the Supplementary material.

Since the present study is focused on the possible influence of VSC on the selectivity between  $\text{P}_1$  and  $\text{P}_2$ , the parameter  $\bar{V}^\ddagger \equiv V_n^\ddagger/x_s^4$  with  $V_n^\ddagger \equiv V^\ddagger/n$  is of particular interest. This is due to the fact that changing the value of  $n$  alters the harmonic frequencies, as shown in Fig. 2, of the various critical points without changing the locations of the reactant well R and the transition states  $\text{TS}_1$  and  $\text{TS}_2$ . Clearly, Fig. 2 shows that decreasing  $V_n^\ddagger$  (increasing  $n$ ) leads to decreasing  $x$ -mode frequencies of all the critical points, while the  $y$ -mode frequencies remain nearly constant. Thus, in the context of VSC, varying  $V_n^\ddagger$  allows one to systematically explore the conditions under which enhancement, suppression, as well as “null” effect on the observable of interest might occur. Thus, the Hamiltonian in Eq. 1 provides a minimal model which enables us to probe how the PES topology and cavity-molecule interactions jointly govern the selectivity.

### Choice of the dipole function and the initial state

The coupling of the cavity mode to the molecular modes is via the dipole function  $\mu(\mathbf{r})$ , and in this work, for simplicity, we assume mainly a dependence on the reaction coordinate  $x$ , unless stated otherwise. In addition, we take a linearized dipole approximation  $\mu(x) \approx \gamma x$ , as is usually done in several such model studies on VSC. The constant  $\gamma$  along with the coupling term  $\lambda_c$  in Eq. 1 determines the Rabi splitting. In Fig. 2(b), we fix  $\lambda_c = 0.1$  a.u, and show the variation of the lowest quantum eigenvalues of the cavity-molecule system with the cavity frequency for one of the parameter value  $V_2^\ddagger$ . The avoided crossing indicates the formation of the polaritons and the corresponding absorption spectrum[62] in Fig. 2(c) for  $\gamma = 1$  yields a Rabi splitting of about  $\sim 100 \text{ cm}^{-1}$ , which is a typical value in the VSC regime[17, 45, 63, 64]. There-

fore, in this study, we fix  $\gamma = 1$  within the linearized dipole approximation.

Following earlier works[39, 41, 65] we choose the initial state to be a polariton wavepacket  $\Psi_0(\mathbf{r}, q_c; t = 0) = \psi(\mathbf{r}; \mathbf{r}_0)\phi(q_c)$  with

$$\psi(\mathbf{r}; \mathbf{r}_0) = \left( \frac{1}{\pi\sigma_x\sigma_y} \right)^{1/2} \exp \left[ -\frac{(x-x_0)^2}{2\sigma_x^2} - \frac{(y-y_0)^2}{2\sigma_y^2} \right], \quad (4)$$

being a minimum uncertainty wavepacket centered at  $\mathbf{r}_0 = (x_0, y_0)$  with width  $\sigma_{x,y} = (\hbar/m\omega_{\text{R}}^{x,y})^{1/2}$  represented as a product of the displaced ground state wavefunction of the harmonized reactant well (along the reaction coordinate  $x$ ) of frequency  $\omega_{\text{R}}^x$  and the ground state wavefunction along the orthogonal coordinate  $y$  of frequency  $\omega_{\text{R}}^y$ . The cavity state

$$\phi(q_c) = \left( \frac{\omega_c}{\pi\hbar} \right)^{1/4} \exp \left[ -\frac{\omega_c q_c^2}{2\hbar} \right] \quad (5)$$

is taken to be the ground state of the harmonic oscillator with frequency  $\omega_c$  and unit mass. Note that for  $\lambda_c \neq 0$ , the above choice of the initial cavity state will lead to the presence of virtual photons inside the cavity. A more appropriate choice[41] that ensures a zero photon cavity state is given by

$$\phi(q_c; \lambda_c) = \left( \frac{\omega_c}{\pi\hbar} \right)^{1/4} \exp \left[ -\frac{\omega_c(q_c - q_{c0})^2}{2\hbar} \right] \quad (6)$$

with  $q_{c0} = -\frac{\lambda_c}{\omega_c}\mu$ . In the following section, we present the results for the virtual photon case. However, qualitatively similar results are obtained for the zero photon case (see Supplementary Sec. S5) as well. The time-evolved state  $\Psi(\mathbf{r}, q_c; t)$  is obtained by numerically solving the Schrödinger equation using the split-operator method. For classical simulations, an ensemble of initial conditions is sampled from the Wigner distribution corresponding to the initial polaritonic wavepacket, and each initial phase space point is then time-evolved by integrating Hamilton’s equations of motion (see Supplementary Sec. S8 for details).

### Observable of interest: branching ratio

The key observable of interest in the context of VSC is the product branching ratio, which is as a measure of the selectivity between the two products  $\text{P}_1$  and  $\text{P}_2$ . In order to calculate the branching ratio one needs to define appropriate domains  $D$  to demarcate reactant and product regions. We use the following definition:

$$D = \begin{cases} \text{R}, & x < 0 \\ \text{P}_1, & x > 0; y < y_{\text{TS}_2} \\ \text{P}_2, & x > 0; y > y_{\text{TS}_2} \end{cases} \quad (7)$$

where the  $\text{TS}_2$  is located at  $(x_{\text{TS}_2}, y_{\text{TS}_2})$ . Although, alternative definitions for  $D$  are possible, the choice above is

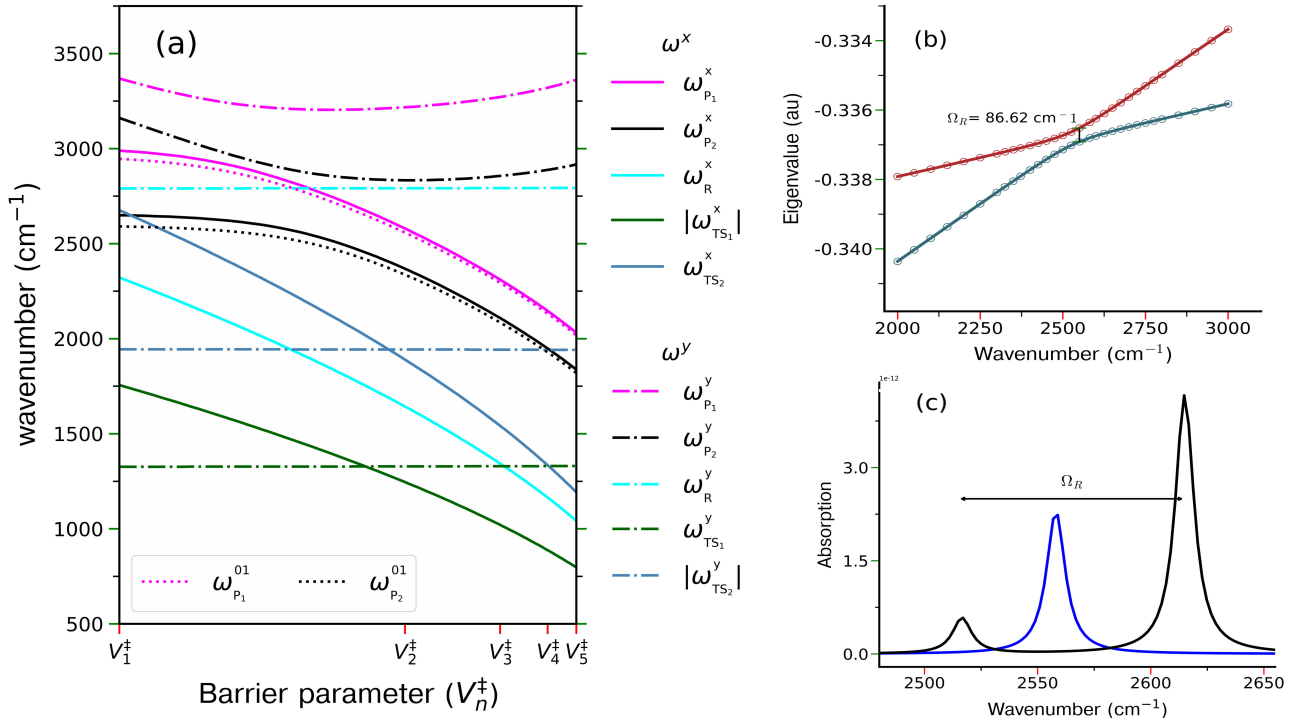


FIG. 2. (a) Variation of the harmonic frequencies associated with the different stationary points (indicated) with the parameter  $V_n^\ddagger$ . Solid and dash-dot lines show the  $x$ -mode and the  $y$ -mode frequencies respectively. In addition, dotted lines show the  $x$ -mode fundamental frequencies ( $0 \rightarrow 1$ ) associated with the two product wells. (b) Variation of the 2<sup>nd</sup> and 3<sup>rd</sup> eigenvalues of Eqn. 1 with cavity frequency  $\omega_c$  for parameter value  $V_2^\ddagger$  exhibiting avoided crossings. (c) show the corresponding absorption spectra[62] in the presence (black) and absence (blue) of cavity-molecule coupling. The cavity-system coupling strength is fixed at  $\lambda_c = 0.1$  a.u.

made for numerical convenience and the results are qualitatively similar with different definitions for the domains. Furthermore, given that our model has no dissipation, we also impose an energetic criterion[58] to mimic the reduction in any thermally induced recrossing between the two product wells. Thus, after the first crossing of TS<sub>1</sub>, if a trajectory enters either the P<sub>1</sub> or P<sub>2</sub> domain and its potential energy falls to  $\sim 3k_B T$  below the TS<sub>2</sub> energy then the trajectory is considered to have formed that specific product. In this work, we set  $T = 300$  K, implying  $3k_B T \sim 2.85 \times 10^{-3}$  a.u., and note that the main results of this work are fairly insensitive to the choice of this cutoff (see Supplementary Fig. S7).

With the definitions above, we calculate the classical time-dependent domain probability as

$$\text{Prob}_D^{CM}(t) = \frac{\mathcal{N}_D(t)}{\mathcal{N}_{tot}}$$

where  $\mathcal{N}_D(t)$  is the number of trajectories in the domain  $D$  and  $\mathcal{N}_{tot}$  is the total number of trajectories. Quantum mechanically, the corresponding domain probability is given by

$$\text{Prob}_D^{QM}(t) = \iint_D |\Psi(\mathbf{r}, q_c; t)|^2 d\mathbf{r} dq_c \quad (8)$$

The respective time-averaged domain probabilities are calculated as follows

$$\bar{\mathcal{P}}_D = \frac{1}{T_{tot}} \int_0^{T_{tot}} \text{Prob}_D(t) dt \quad (9)$$

where  $T_{tot}$  is the total propagation time. In the results presented below, we take  $T_{tot} = 1$  ps and note that qualitatively similar results are obtained for larger  $T_{tot}$  as well (see Supplementary Sec. S2). The time-averaged domain probabilities allow us to define the branching ratio (selectivity)

$$\mathcal{B}(\bar{V}^\ddagger, \lambda_c, \omega_c) = \frac{\bar{\mathcal{P}}_{P_1}}{\bar{\mathcal{P}}_{P_2}} \quad (10)$$

Since the asymmetry parameter is fixed at  $\alpha = 0.1$ ,  $\mathcal{B}$  can be different from unity even in the absence of coupling ( $\lambda_c = 0$ , see Supplementary Fig. S5) to the cavity. Therefore, we define the normalized branching ratio

$$\bar{\mathcal{B}}(\bar{V}^\ddagger, \lambda_c, \omega_c) \equiv \frac{\mathcal{B}(\bar{V}^\ddagger, \lambda_c, \omega_c)}{\mathcal{B}(\bar{V}^\ddagger, 0, \omega_c)} \quad (11)$$

as a measure of the extent to which VSC modulates the branching ratio.

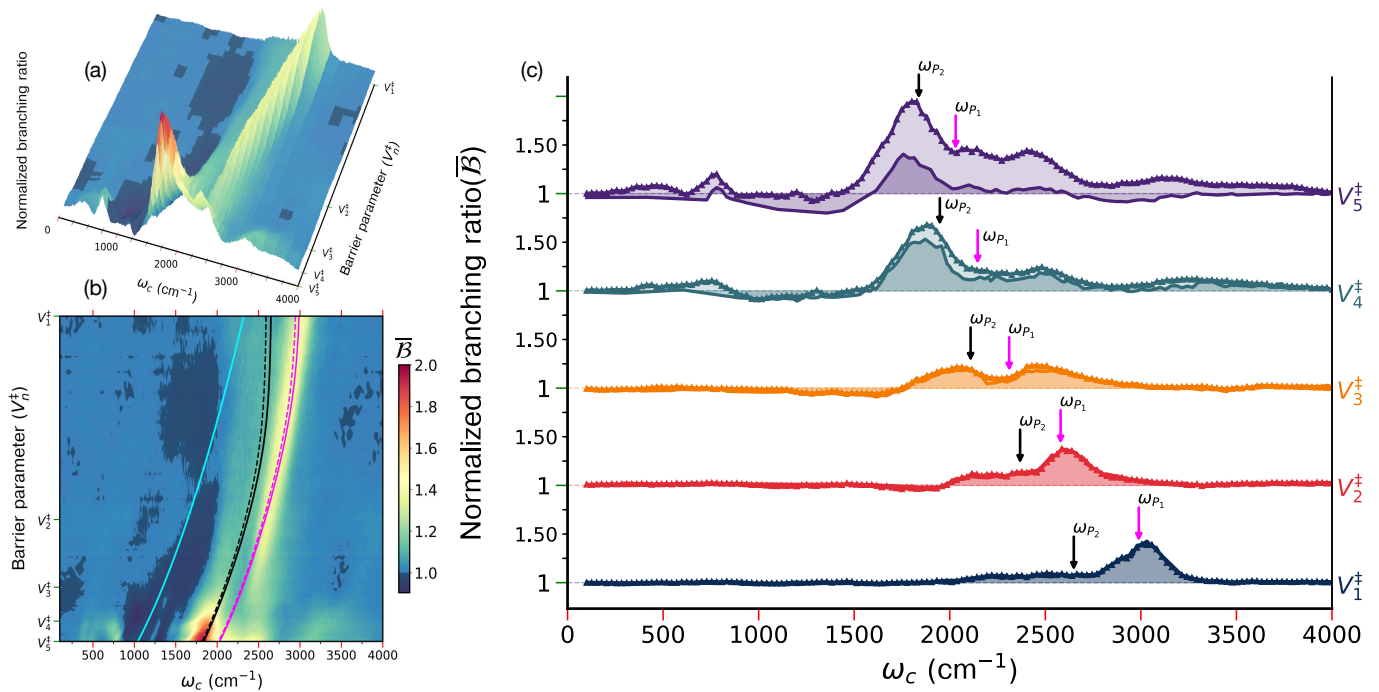


FIG. 3. (a) and (b) Two different representations of the classical normalized branching ratio Eq. 11 as a function of the cavity frequency  $\omega_c$  and barrier parameter  $V_n^\ddagger$ . The landscape is computed on a  $311 \times 100$  grid (see supplementary for details on the grid setup) for an initial state with energy  $\langle E_S \rangle \approx 0.01$  a.u. with the cavity-system coupling strength  $\lambda_c = 0.1$  a.u. and asymmetry parameter  $\alpha = 0.1$ . In (b) the varying harmonic (solid lines) and fundamental (dashed lines) frequencies of the reactant well  $\omega_R^x$  (cyan), the deeper product well  $\omega_{P_1}^x$  (magenta), and the product well  $\omega_{P_2}^x$  (black) are superimposed. (c) Classical (lines with symbols) and quantum (solid lines) branching ratios for specific  $V_n^\ddagger$  values. The  $x$ -mode harmonic frequencies for the two product wells are indicated with arrows.

## RESULTS AND DISCUSSION

In what follows, we choose the center of the matter wavepacket  $(x_0, y_0) = (-0.85, 0.016)$  a.u., corresponding to the average system energy  $\langle E_S \rangle = \langle \psi | H_M | \psi \rangle \approx 0.01$  a.u. This energy is above that of the  $\text{TS}_1$  saddle ( $E_{\text{TS}_1} = 0$ ) and chosen in order to facilitate a classical-quantum comparison of the VSC effect. Although, for the specific choice of the initial wavepacket,  $\langle E_S \rangle$  does depend on the parameter  $V_n^\ddagger$ , the variations are small over the range of interest (see Supplementary Fig. S4). Note that the main features of our results remain invariant for other choices of  $\langle E_S \rangle$  values (Supplementary Sec. S3).

### Establishing the VSC effect

The central results of our computations are summarized in Fig. 3 wherein the classical branching ratio  $\bar{B}(V_n^\ddagger, \lambda_c, \omega_c)$  is shown as a function of the cavity frequency  $\omega_c$  and the parameter  $V_n^\ddagger$  which controls the depths and the fundamental frequencies of the reactant and product wells. Essentially, Figs. 3(a) and (b) show the “VSC landscape” for our model system and one can clearly observe specific regions on this landscape exhibiting significant variations in the branching ratio. Three

key observations can be made:

- A ridge of enhanced  $\bar{B}$  can be seen starting from  $V_1^\ddagger$  at around  $\omega_c \sim 3000 \text{ cm}^{-1}$  and persisting up until nearly  $V_3^\ddagger$  with  $\omega_c \sim 2500 \text{ cm}^{-1}$ .
- Beyond  $V_3^\ddagger$ , as the barrier parameter is decreased, the ridge bifurcates with a prominent, and maximal for this study, enhancement in the branching ratio around  $\omega_c \sim 1800 \text{ cm}^{-1}$  for  $V_5^\ddagger$ .
- The comparison between classical and quantum  $\bar{B}$  for select  $V_n^\ddagger$  shown in Fig. 3(c) indicates that the initial ridge structure is reproduced quantum mechanically as well. Importantly, despite quantitative differences, the cavity frequencies at which significant modulation of  $\bar{B}$  occurs remain nearly invariant in the quantum and classical cases.

Are the modulations of selectivity noted above due to VSC? The answer is in the affirmative, and this can be seen from Fig. 3(b) where we have superimposed the  $x$ -mode harmonic frequencies corresponding to the reactant and the two products onto the VSC landscape. It is immediately clear that the initial ridge structure corresponds to the resonance  $\omega_c \sim \omega_{P_1}^x$  between the cavity frequency and the harmonic frequency of the  $P_1$  product

well. Significantly, the ridge structure nearly follows the variation of  $\omega_{P_1}^x$  with  $V_n^\ddagger$  seen in Fig. 2, thus implying the robustness of the resonance effect. Interestingly, the bifurcation of the ridge leading to a shift of the maximum in  $\bar{B}$  starting from  $V_4^\ddagger$  corresponds to the resonance  $\omega_c \sim \omega_{P_2}^x$  involving the cavity mode and the harmonic frequency of the shallower  $P_2$  product well. This observation is surprising, and perhaps counterintuitive as well, since VSC of the cavity mode with the shallower well (“minor product”) results in an increased selectivity of the deeper well (“major product”). Thus, depending on the relative depths of the product wells, the VSC effect exhibits a switch in the resonant frequency. At this stage it is worth mentioning that the observed resonant enhancements of  $\bar{B}$  are robust under variations of various system parameters (see Supplementary sec. S2 and S3) and the off-cavity branching ratio varies very little over the entire range of  $V_n^\ddagger$  (see Supplementary Fig. S5).

In order to examine the VSC effect in more detail, Fig. 3(c) shows slices of the landscape at specific  $V_n^\ddagger$  values. For  $V_1^\ddagger$ , the normalized branching ratio  $\bar{B}$  shows a peak around  $\omega_c \sim \omega_{P_1}^x$  and the peak persists at  $V_2^\ddagger$ , but with slightly reduced intensity. For  $V_3^\ddagger$ , the picture becomes more complex with  $\bar{B}$  exhibiting two peaks corresponding to nearly the same enhancement. The second new peak nearly corresponds to  $\omega_c \sim \omega_{P_2}^x$  resonance whereas the first peak is blue-shifted from the  $\omega_c \sim \omega_{P_1}^x$  resonance, indicating competing resonant pathways. At  $V_4^\ddagger$  the maximal enhancement of  $\bar{B}$  appears around the resonance  $\omega_c \sim \omega_{P_2}^x$  and this trend is amplified at  $V_5^\ddagger$ , where the branching ratio is nearly twice that of the off-cavity case. In addition, for both the  $V_4^\ddagger$  and  $V_5^\ddagger$  cases the enhancement in selectivity at  $\omega_c \sim \omega_{P_1}^x$  appears to be part of a rather broad shoulder-like feature. In addition, as seen from Fig. 3(b) as well as Fig. 2, since the harmonic frequencies corresponding to the two product wells are fairly close to their fundamental frequencies, the observed resonance shift is not due to anharmonic effects. Importantly, at all values of  $V_n^\ddagger$  the system continues to prefer  $P_1$ ; what changes is the cavity frequency at which this preference is most strongly enhanced.

Another key point to be noted at this stage is that the branching ratios in Fig. 3(c) exhibit good classical-quantum correspondence in terms of the resonance frequencies as well as the shift of the dominant enhancement frequency. Consequently, this indicates that the primary mechanism governing the cavity-modified selectivity is largely classically in origin and arises from the dynamical steering in the post transition state region. Nevertheless, quantitative differences between classical and quantum  $\bar{B}$  can be seen for  $V_4^\ddagger$  and  $V_5^\ddagger$  with the latter exhibiting a reduced enhancement for  $\omega_c \sim \omega_{P_2}^x$  when compared to the classical result. A possible explanation for this has to do with quantum tunneling between the product wells and the resulting partial delocalization of the wavepacket. However, in this work we do not further analyze such effects.

## Mechanism for the enhancement of selectivity

A possible explanation for the results shown in Fig. 3 involves a cavity coupling mediated changes in the nature of the intrinsic reaction coordinate (IRC). Indeed, as shown in Fig. 4, varying  $V_n^\ddagger$  results in the IRC moving away from  $TS_2$  and almost exclusively leading to the product  $P_1$ . If this assumption holds, then one should observe a monotonic increase in the selectivity  $\bar{B}$  at the cavity-molecule resonance  $\omega_c \sim \omega_{P_1}^x$ . However, the results shown in Fig. 3(c) contradict this expectation. In particular, apart from the reduction in  $\bar{B}$  for  $V_3^\ddagger$ , the observation of a different resonance  $\omega_c \sim \omega_{P_2}^x$  leading to the maximal enhancement in the selectivity of  $P_1$  for  $V_4^\ddagger$  and  $V_5^\ddagger$  cannot be explained by arguments based solely on the change in the IRC. Thus, the resonant modulations in the selectivity of the coupled cavity-system case must be due to dynamical effects.

An important clue emerges from Fig. 5 wherein the time averaged product well domain probabilities are shown. These results should be compared to the branching ratios shown in Fig. 3(c) since it is the ratio of the domain probabilities that yield the branching ratios. For cavity frequencies away from the resonant frequencies, Fig. 5 shows that the  $\bar{P}_D$  for both the product wells is influenced by the cavity but varies to a similar extent. Thus, for such cavity frequencies, the branching ratio in Fig. 3(c) remains close to unity. However, for  $\omega_c$  near the  $TS_2$  transverse frequency  $\omega_{TS_2}^x$ , the  $P_2$  well domain probabilities begin to decrease while the  $P_1$  well domain probabilities keep increasing until  $\omega_c \sim \omega_P^x$ . Consequently, the substantial difference in the domain probabilities of the two wells at  $\omega_c \sim \omega_P^x$  gives rise to the resonant enhancements seen in Fig. 3(c). Given that earlier studies[41, 59, 66] have emphasized the key role of the cavity in post transition state cooling into the product well, the results in Fig. 5 suggest that analyzing the resonant cavity-system energy exchange is necessary to rationalize the observed enhancement in selectivity.

### Coherent cavity-system energy exchange

In order to examine the cavity-system energy exchange dynamics, we begin by showing in Fig. 6(a) and (b) the average system and cavity energies (see Supplementary Sec. S6 for definitions) in the off and on resonance scenario for  $V_2^\ddagger$  and  $V_4^\ddagger$  cases respectively. Note that both classical and quantum results are compared with appropriate initial states that were utilized to obtain the branching ratios shown in Fig. 3. Apart from the striking classical-quantum correspondence, one can observe a clear difference in the average energies when the cavity is on and off resonant with the product well  $x$ -mode frequencies. While there is some cavity-system energy exchange in the off-resonant cases, the on-resonance cases show a substantial cooling of the system over timescales

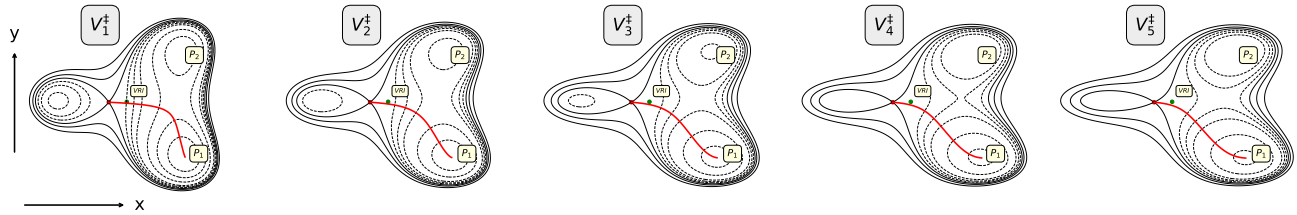


FIG. 4. Intrinsic reaction coordinate (IRC, red curve) projected onto the two-dimensional PES for varying barrier parameter  $\bar{V}^\ddagger = V_n^\ddagger/x_s^4 \equiv V^\ddagger/nx_s^4$  with  $n = 1, \dots, 5$ .

of a few hundred femtoseconds. This cooling of the system clearly correlates with the cavity gaining energy and hence establishes the active cavity-system energy exchange for  $\omega_c \sim \omega_{P_1}^x$  and  $\omega_c \sim \omega_{P_2}^x$  cases. Note that for the choice of the off-resonant frequencies in Fig. 6(a) and (b), one observes, despite the influence of the cavity on the domain probabilities in Fig. 5, a near unit branching ratio.

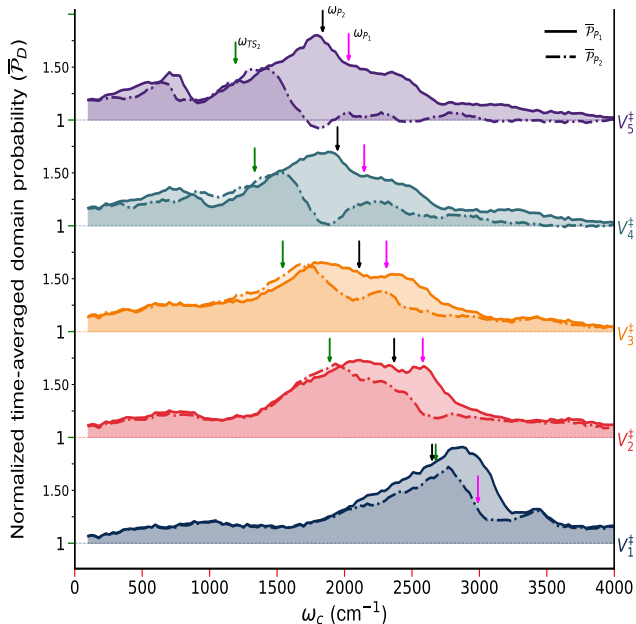


FIG. 5. Classical normalized time averaged domain probabilities Eq. 9 corresponding to the branching ratios shown in 3(c). Apart from the  $x$ -mode frequencies of the product wells, the transverse mode frequency at  $TS_2$  is also indicated (green arrow).

For gaining further insights into the on-resonance cooling of the system seen in Fig. 6(a) and (b), we analyze the detailed classical dynamics of the model system. An ensemble of 20000 initial trajectories is sampled at the first transition state  $TS_1$  with the condition  $p_x > 0$  for a fixed system energy of  $E_s = 0.01$  a.u. and the cavity mode being in its ground state. Thus, in terms of the cavity action-angle variables, the cavity action is fixed at  $J_c = 0.5$ , while the angle variable  $\theta_c$  is randomly chosen

from the interval  $[0, 2\pi]$ . We then propagate Hamilton's equations of motion, ensuring proper convergence of the results.

In Fig. 6(c)-(f), we show the time evolution of the various energies for representative example trajectories in on and off resonance cases. Note that similar qualitative behaviour is seen for several other trajectories as well. To track the time evolution in terms of the various domains that are visited, we assign a ‘‘domain tag’’ which is assigned values of 1, 2, and 0 when the trajectory enters the  $P_1$ ,  $P_2$ , and the  $R$  wells, respectively. Further, a value of 1.5 is assigned when the trajectory is not in any of the three wells, but in some intermediate regions. Such an analysis is useful in providing information, not readily available from the average energy results shown in Fig. 6, about the regions where dominant cooling of the system is observed. The off-resonance cases for  $V_2^\ddagger$  and  $V_4^\ddagger$  are shown in Figs. 6(c) and (d), respectively, along with the domain tag of the trajectory. In these cases, it is clear that the energy exchanged between the system and the cavity mode is relatively small and incoherent. The domain tags show frequent interwell transitions between the two product wells and no visits to the reactant well over the timescale of interest. In contrast, under on-resonance conditions shown in Figs. 6(e) and (f), one can clearly see significant and coherent cavity-system energy transfer over a timescale of  $\sim 200$  fs. More importantly, when the trajectory enters either of the product wells, it remains trapped for an extended duration in that well, as indicated by the domain tag, during which a substantial amount of energy is transferred from the system to the cavity mode, leading to cooling. Subsequently, as has been observed earlier[47], the cavity returns the energy back to the system as the trajectory exits out of that specific product well. These repeated, synchronized energy transfer events indicate a coherent exchange between the reaction coordinate and the cavity mode during each trapping episode.

Thus, an interesting consequence of our computations is that, irrespective of the well which is involved in VSC, substantial cooling occurs in both the product wells. Although the mechanism for the observed cooling of both wells for a single resonant frequency is not clear at present, we suspect that resonance between the nonlinear mode frequencies of the system and the cavity fre-

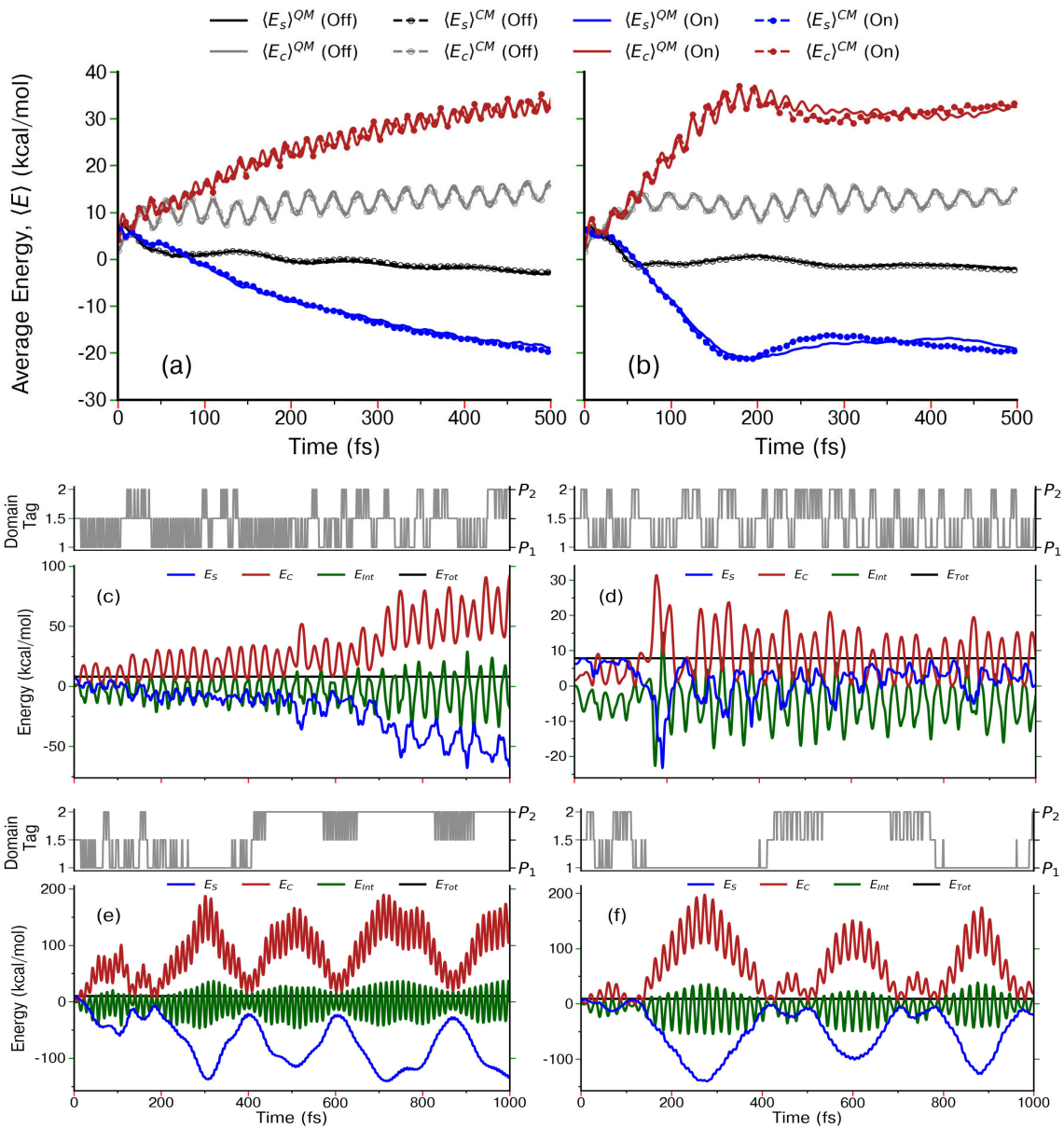


FIG. 6. Average energies (indicated in the legend) as a function of time for (a)  $V_2^\ddagger$  with  $\omega_c = 1200 \text{ cm}^{-1}$  (off resonance),  $\omega_c = \omega_{P_1}^x = 2586 \text{ cm}^{-1}$  (on resonance) and (b)  $V_4^\ddagger$  with  $\omega_c = 1071 \text{ cm}^{-1}$  (off resonance),  $\omega_c = \omega_{P_2}^x = 1871 \text{ cm}^{-1}$  (on resonance). Solid lines show the quantum and dotted lines with markers show the classical results. (c) and (d) Energy variations (lower panels) for sample classical trajectories at off resonance cavity frequencies for  $V_2^\ddagger$  and  $V_4^\ddagger$  respectively, and (e) and (f) shows energy variations for sample classical trajectories at on resonance cavity frequencies for  $V_2^\ddagger$  and  $V_4^\ddagger$  respectively. Domain tags (upper panel) of 1, 2, 0 and 1.5 indicating whenever a trajectory enters  $P_1$ ,  $P_2$ ,  $R$  wells, and outside all three wells, respectively. All computations are shown for cavity-system coupling strength  $\lambda_c = 0.1 \text{ au}$  and  $\alpha = 0.1$

quency plays an important role. Preliminary evidence towards this is provided in the Supplementary Sec. S7 in terms of a wavelet based time-frequency analysis of the dynamics. At the same time Supplementary Sec. S7 also provides evidence for significant change in the extent of regularity under VSC which correlates with the observed variations in the branching ratios with varying cavity frequency. Thus, there are indications towards emergence of resonant structures in the product well phase space

regions[41].

#### *Insights into the VSC frequency switching*

A key observation from Fig. 3(c) was the fact that the branching ratio peak switched from  $\omega_c \sim \omega_{P_1}^x$  to  $\omega_c \sim \omega_{P_2}^x$  as the barrier parameter is tuned from  $V_1^\ddagger$  to  $V_5^\ddagger$ .

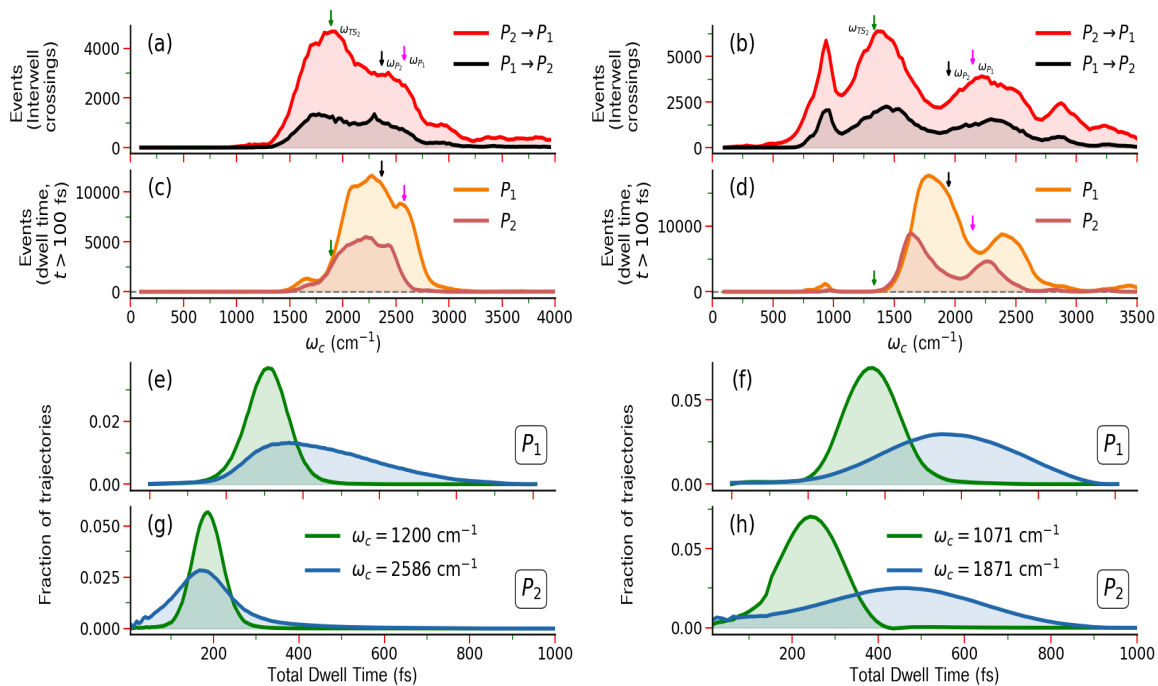


FIG. 7. (a) and (c) Number of trajectories undergoing  $P_1 \leftrightarrow P_2$  inter-well transitions and exhibiting dwell times in the product wells for at least 100 fs respectively as a function of the cavity frequency for  $V_2^\ddagger$ . (b) and (d) show the corresponding results for  $V_4^\ddagger$  case. (e) and (g) show the product well dwell time distributions for  $V_2^\ddagger$  in the resonant (blue) and off-resonant (green) cases. The corresponding results for  $V_4^\ddagger$  are shown in (f) and (h). Note that for (e)-(h) an ensemble size of  $10^5$  trajectories is used.

This, as pointed out above, approximately correlates with the observations in Fig. 5 wherein, in the vicinity of the  $TS_2$  transverse frequency, the domain probability of the shallower  $P_2$  well decreases while the deeper well domain probability continues to increase. Given that both wells undergo cooling, and hence trap population, this suggests that interwell  $P_1 \leftrightarrow P_2$  transitions are playing a key role with changing  $V_n^\ddagger$ .

In order to highlight the role of the interwell transitions, in Fig. 7(a) and (b) we show the statistics of the  $P_1 \leftrightarrow P_2$  transitions for  $V_2^\ddagger$  and  $V_4^\ddagger$  cases respectively as a function of the cavity frequency. The computations are done as follows: once a trajectory enters one of the wells, an interwell crossing event is counted if the trajectory transitions to the other well and stays trapped for  $\sim 20$  fs, which is the timescale associated with the  $TS_2$  barrier curvature. It is immediately clear that for  $V_4^\ddagger$  far more interwell transitions happen and, interestingly, even the peak in the interwell transitions around  $\omega_c \sim 900$  cm $^{-1}$  appears to correlate with the small enhancement of the branching ratio seen in Fig. 3(c). The reason for the increased interwell transitions is due to the change in the shape of the PES – upon changing the barrier parameter from  $V_2^\ddagger$  to  $V_4^\ddagger$  the transition state  $TS_2$  and reactant well  $R$  come energetically close (see Supplementary Fig. S2 bottom row and S3) and, as seen from Fig. 2(a), the transverse frequency  $\omega_{TS_2}^x$  decreases. This results in a

relatively flat region of the PES after the VRI point and, given that cooling can occur in both wells, the increased  $P_2 \rightarrow P_1$  transitions can lead to long time trapping in the  $P_1$  well when  $\omega_c \sim \omega_{P_1}^x$  or  $\omega_{P_2}^x$ . This can be seen from Fig. 7(c) and (d) which show the fraction of trajectories that get trapped in the product wells for 100 fs or more. Note that, by construction, the interwell transitions capture the short timescale dynamics, whereas the results in Fig. 7(c) and (d) account for the long time dynamics due to the VSC effect.

Insights into the frequency switching come from a closer inspection of Figs. 7(c)-(h), where key differences between the  $V_2^\ddagger$  and  $V_4^\ddagger$  cases emerge. In the case of  $V_2^\ddagger$  shown in Fig. 7(c) the fraction of long time trapped trajectories peaks around  $\omega_c \sim \omega_{P_2}^x$  for both product wells. However, since  $P_1$  is deeper than the  $P_2$  well, the fraction is considerably larger for the deeper well. Around the same cavity frequency the  $P_1 \rightarrow P_2$  transitions decrease precipitously. At  $\omega_c \sim \omega_{P_1}^x$  resonance, the trapping or dwell time distributions shown in Fig. 7(e) and (g) indicate that the  $P_1$  well traps population more effectively when compared to the  $P_2$  well. Consequently, the combination of reduced interwell transitions at this frequency and the efficient cooling in the  $P_1$  well result in the branching ratio peak at  $\omega_c \sim \omega_{P_1}^x$  in Fig. 3(c). In contrast, for the  $V_4^\ddagger$  case Fig. 7(d) exhibits a peak in the long time trapped fraction around the resonance  $\omega_c \sim \omega_{P_2}^x$

whereas the corresponding population in the  $P_2$  well is comparatively much smaller. Interestingly, Figs. 7(g) and (h) indicate that in this instance the  $P_2$  well can also trap population effectively at resonance. Nevertheless, the shallowness of the  $P_2$  well leads to increased  $P_2 \rightarrow P_1$  transitions around  $\omega_c \sim \omega_{P_2}^x$ , as evident from Fig. 7(b) and hence a much more rapid loss in the fraction of long time trapped trajectories in the shallow well. The net effect can be seen in Fig. 3(c) as a peak around  $\omega_c \sim \omega_{P_2}^x$  in the branching ratio.

## CONCLUSION

The potential for VSC to modulate reactions in a mode-specific manner is crucially dependent on our understanding of the cavity-induced mechanistic changes in the reaction dynamics. A prime aspect in this context depends on our ability to correlate possible effects of VSC with the complex features that are typically found on multidimensional PES. In this work, by utilizing detailed classical and quantum dynamics on a model system exhibiting post-transition state bifurcation (PTSB), we have established that VSC can influence the selectivity between major and minor products of a chemical reaction. Moreover, by varying a single parameter that controls the shape of the PES, we have illustrated the robustness of our observations and that the cavity with an appropriately tuned frequency effectively acts as an engineered vibrational bath that facilitates “cooling down” of the system. Note that the cooling of the system under resonant VSC has been invoked before[47, 59, 66] with emphasis on the dynamical nature of the rate modulations. A new aspect of our work is that the cooling occurs in both the product wells even if the cavity frequency is resonant with only one of the product well’s fundamental transition.

Apart from a good classical-quantum correspondence for the branching ratios, our study also underscores the complexity of the VSC phenomenon. Firstly, the cavity frequency at which a maximal VSC response is expected can change with the shape of the PES and this seems to be related to the fact that both the product wells can trap population under a single resonance condition. Secondly, our observations on the branching ratio and the corresponding domain probabilities emphasize an important point – strong coupling to the cavity does alter the

dynamics even though a highly averaged or composite observable like reaction rate or branching ratio does not appear to change under VSC. In this context, we mention that the influence of the cavity on selectivity in an electrophilic reaction has been shown[67] even in the non-resonant regime. Thus, these results highlight the potential of VSC as a powerful means of steering reaction outcomes in systems exhibiting PTSB.

Although the present study focuses on a single-molecule reaction coupled to a single cavity mode, it provides a necessary starting point for exploring additional effects that arise in realistic settings, such as in the collective limit[68, 69] and in the presence of dissipation and cavity losses[18, 31, 32, 45, 70]. Related to this is the question of whether a single-mode cavity description remains adequate, or whether multiple cavity modes, present in experiments, must be explicitly taken into account. At this stage, the persistence of the single-molecule, single-mode control mechanism in the collective limit and in multimode cavity environments is difficult to assess definitively. Nevertheless, the central physical insight emerging from this study — namely, that a properly tuned cavity mode can act as an effective vibrational “bath” that resonantly cools and stabilizes the system in a selected product well is expected to remain robust under these more complex conditions, provided that solvent-induced dissipation is not too strong. However, following the early work[71] by Ke and Assan, the presence of multiple cavity modes may further enhance this effect by offering additional channels for vibrational energy redistribution. Finally, we note that a recent study[72] by Mondal *et al.* shows that several crucial insights of the VSC induced effects can be obtained from consideration of the many-body nature of the VSC. It remains to be seen if such viewpoint can be extended to PESs exhibiting complex features discussed here.

## ACKNOWLEDGEMENTS

S.M. is grateful to the Ministry of Education, Government of India, for the Prime Minister Research Fellowship (PMRF) and the Fellowship for Academic and Research Excellence (FARE). A.K. thanks IIT Kanpur for the fellowship and the High Performance Computing (HPC) Center at IIT Kanpur for providing computing resources.

- 
- [1] T. Uzer and W. Miller, Theories of intramolecular vibrational energy transfer, *Phys. Rep.* **199**, 73 (1991).
  - [2] K. K. Lehmann, G. Scoles, and B. H. Pate, Intramolecular dynamics from eigenstate-resolved infrared spectra, *Annu. Rev. Phys. Chem.* **45**, 241 (1994).
  - [3] D. J. Nesbitt and R. W. Field, Vibrational energy flow in highly excited molecules: role of intramolecular vibrational redistribution, *J. Phys. Chem.* **100**, 12735 (1996).
  - [4] S. K. Lee, A. G. Suits, H. B. Schlegel, and W. Li, A reaction accelerator: Mid-infrared strong field dissociation yields mode-selective chemistry, *J. Phys. Chem. Lett.* **3**, 2541 (2012).
  - [5] L. Windhorn, J. S. Yeston, T. Witte, W. Fuß, M. Motzkus, D. Proch, K.-L. Kompa, and C. B. Moore, Getting ahead of IVR: A demonstration of mid-infrared induced molecular dissociation on a sub-statistical time

- scale, *J. Chem. Phys.* **119**, 641 (2003).
- [6] M. Gruebele and P. G. Wolynes, Vibrational energy flow and chemical reactions, *Acc. Chem. Res.* **37**, 261 (2004).
- [7] D. M. Leitner, Quantum ergodicity and energy flow in molecules, *Adv. Phys.* **64**, 445 (2015).
- [8] S. Karmakar and S. Keshavamurthy, Intramolecular vibrational energy redistribution and the quantum ergodicity transition: a phase space perspective, *Phys. Chem. Chem. Phys.* **22**, 11139 (2020).
- [9] A. Maitra, S. Sarkar, D. M. Leitner, and J. M. Dawlaty, Electric fields influence intramolecular vibrational energy relaxation and line widths, *J. Phys. Chem. Lett.* **12**, 7818 (2021).
- [10] P. H. Shaon, H. Poudel, and D. M. Leitner, Tuning vibrational lifetimes by chemical substitution and impact on plasmon-assisted catalysis, *J. Phys. Chem. A* **129**, 2006 (2025).
- [11] M. Hassani, P. H. Shaon, C. J. Mallon, T. Shi, J. N. Monzy, E. E. Fenlon, D. M. Leitner, and M. J. Tucker, Modulating vibrational energy redistribution in highly conjugated systems, *J. Chem. Phys.* **162** (2025).
- [12] A. J. Schmitz, H. D. Pandey, F. Chalyavi, T. Shi, E. E. Fenlon, S. H. Brewer, D. M. Leitner, and M. J. Tucker, Tuning molecular vibrational energy flow within an aromatic scaffold via anharmonic coupling, *J. Phys. Chem. A* **123**, 10571 (2019).
- [13] S. R. Rather, M. J. Bezdek, P. J. Chirik, and G. D. Scholes, Dinitrogen coupling to a terpyridine-molybdenum chromophore is switched on by fermi resonance, *Chem* **5**, 402 (2019).
- [14] G. Czakó, B. Gruber, D. Papp, V. Tajti, D. A. Tasi, and C. Yin, First-principles mode-specific reaction dynamics, *Phys. Chem. Chem. Phys.* **26**, 15818 (2024).
- [15] A. Thomas, J. George, A. Shalabney, M. Dryzhakov, S. J. Varma, J. Moran, T. Chervy, X. Zhong, E. Devaux, C. Genet, *et al.*, Ground-state chemical reactivity under vibrational coupling to the vacuum electromagnetic field, *Angew. Chem. Int. Ed.* **128**, 11634 (2016).
- [16] A. Thomas, L. Lethuillier-Karl, K. Nagarajan, R. M. Vergauwe, J. George, T. Chervy, A. Shalabney, E. Devaux, C. Genet, J. Moran, *et al.*, Tilting a ground-state reactivity landscape by vibrational strong coupling, *Science* **363**, 615 (2019).
- [17] K. Nagarajan, A. Thomas, and T. W. Ebbesen, Chemistry under vibrational strong coupling, *J. Am. Chem. Soc.* **143**, 16877 (2021).
- [18] W. Ahn, J. F. Triana, F. Recabal, F. Herrera, and B. S. Simpkins, Modification of ground-state chemical reactivity via light-matter coherence in infrared cavities, *Science* **380**, 1165 (2023).
- [19] K. Hirai, J. A. Hutchison, and H. Uji-i, Recent progress in vibropolaritonic chemistry, *ChemPlusChem* **85**, 1981 (2020).
- [20] J. Lather, P. Bhatt, A. Thomas, T. W. Ebbesen, and J. George, Cavity catalysis by cooperative vibrational strong coupling of reactant and solvent molecules, *Angew. Chem. Int. Ed.* **131**, 10745 (2019).
- [21] M. K. Mahato, K. S. Mony, H. Baliyan, S. Biswas, and A. Thomas, Exploring excited state proton transfer in thin films under vibrational strong coupling, *Angew. Chem.* **137**, e202424247 (2025).
- [22] S. Kumar, S. Biswas, U. Rashid, K. S. Mony, G. Chandrasekharan, F. Mattiotti, R. M. Vergauwe, D. Hagemuller, V. Kaliginedi, and A. Thomas, Extraordinary electrical conductance through amorphous nonconducting polymers under vibrational strong coupling, *J. Am. Chem. Soc.* **146**, 18999 (2024).
- [23] P. Zheng, S. Semancik, and I. Barman, Quantum vibropolaritonic sensing, *Sci. Adv.* **11**, eady7670 (2025).
- [24] B. Xiang and W. Xiong, Molecular polaritons for chemistry, photonics and quantum technologies, *Chem. Rev.* **124**, 2512 (2024).
- [25] M. Dang, S. Maiti, A. Chakraborty, G. M. Kothapalli, and K. Nagarajan, Altering glass transition in polymer films through vibrational strong coupling, *J. Phys. Chem. Lett.* **16**, 12361 (2025).
- [26] J. Sepulveda, J. L. Montaña-Priede, J. Aizpurua, and R. Esteban, Semianalytical treatment of collective vibrational strong coupling in infrared phononic and plasmonic nanoantennas, *J. Phys. Chem. C* **129**, 12374 (2025).
- [27] B. Cohn, A. Sribnyi, S. U. Nawagamuwage, J. Zhou, M. Shakeel, I. V. Rubtsov, and L. Chuntonov, Controlling intramolecular vibrational redistribution with an infrared photonic cavity, *J. Phys. Chem. Lett.* **16**, 6551 (2025).
- [28] A. P. Fidler, L. Chen, A. M. McKillop, and M. L. Weichman, Ultrafast dynamics of CN radical reactions with chloroform solvent under vibrational strong coupling, *J. Chem. Phys.* **159**, 164302 (2023).
- [29] L. Chen, A. P. Fidler, A. M. McKillop, and M. L. Weichman, Exploring the impact of vibrational cavity coupling strength on ultrafast CN+ c-C6H12 reaction dynamics, *Nanophotonics* **13**, 2591 (2024).
- [30] C. Muller, M. Piejko, S. Bascil, and J. Moran, The diels-alder reaction as a mechanistic probe for vibrational strong coupling, *Angew. Chem. Int. Ed.* **64**, e202509391 (2025).
- [31] L. P. Lindoy, A. Mandal, and D. R. Reichman, Quantum dynamical effects of vibrational strong coupling in chemical reactivity, *Nat. Commun.* **14**, 2733 (2023).
- [32] Y. Ke and J. O. Richardson, Quantum nature of reactivity modification in vibrational polariton chemistry, *J. Chem. Phys.* **161**, 054104 (2024).
- [33] M. R. Fiechter, J. E. Runeson, J. E. Lawrence, and J. O. Richardson, How quantum is the resonance behavior in vibrational polariton chemistry?, *J. Phys. Chem. Lett.* **14**, 8261 (2023).
- [34] K. Schwenicke, A. Koner, J. B. Pérez-Sánchez, W. Xiong, N. C. Giebink, M. L. Weichman, and J. Yuen-Zhou, When do molecular polaritons behave like optical filters?, *Chem. Soc. Rev.* **54**, 6482 (2025).
- [35] T. E. Li, A. Nitzan, and J. E. Subotnik, Collective vibrational strong coupling effects on molecular vibrational relaxation and energy transfer: Numerical insights via cavity molecular dynamics simulations, *Angew. Chem. Int. Ed.* **133**, 15661 (2021).
- [36] C. Schäfer, J. Flick, E. Ronca, P. Narang, and A. Rubio, Shining light on the microscopic resonant mechanism responsible for cavity-mediated chemical reactivity, *Nat. Commun.* **13**, 7817 (2022).
- [37] T. T. Chen, M. Du, Z. Yang, J. Yuen-Zhou, and W. Xiong, Cavity-enabled enhancement of ultrafast intramolecular vibrational redistribution over pseudorotation, *Science* **378**, 790 (2022).
- [38] T. E. Li and S. Hammes-Schiffer, QM/MM modeling of vibrational polariton induced energy transfer and chemical dynamics, *J. Am. Chem. Soc.* **145**, 377 (2022).

- [39] S. Mondal, D. S. Wang, and S. Keshavamurthy, Dissociation dynamics of a diatomic molecule in an optical cavity, *J. Chem. Phys.* **157**, 244109 (2022).
- [40] J. A. Gómez and O. Vendrell, Vibrational energy redistribution and polaritonic fermi resonances in the strong coupling regime, *J. Phys. Chem. A* **127**, 1598 (2023).
- [41] S. Mondal and S. Keshavamurthy, Phase space perspective on a model for isomerization in an optical cavity, *J. Chem. Phys.* **159**, 074106 (2023).
- [42] Q. Yu and J. M. Bowman, Manipulating hydrogen bond dissociation rates and mechanisms in water dimer through vibrational strong coupling, *Nat. Commun.* **14**, 3527 (2023).
- [43] S. Mondal and S. Keshavamurthy, Cavity induced modulation of intramolecular vibrational energy flow pathways, *J. Chem. Phys.* **161**, 194302 (2024).
- [44] Q. Yu, D. H. Zhang, and J. M. Bowman, Theoretical and quantum mechanical deconstruction of vibrational energy transfer pathways modified by collective vibrational strong coupling, *Nat. Commun.* **16**, 6760 (2025).
- [45] W. Ying and P. Huo, Resonance theory of vibrational strong coupling enhanced polariton chemistry and the role of photonic mode lifetime, *Commun. Mat.* **5**, 110 (2024).
- [46] C. Schafer, J. Fojt, E. Lindgren, and P. Erhart, Machine learning for polaritonic chemistry: Accessing chemical kinetics, *J. Am. Chem. Soc.* **146**, 5402 (2024).
- [47] S. M. Garner, X. Li, and S. Hammes-Schiffer, Simulation of vibronic strong coupling and cavity-modified hydrogen tunneling dynamics, *J. Chem. Phys.* **163**, 134113 (2025).
- [48] X. Ji and T. E. Li, Selective excitation of ir-inactive modes via vibrational polaritons: Insights from atomistic simulations, *J. Phys. Chem. Lett.* **16**, 5034 (2025).
- [49] R. M. Minyaev, Gradient lines on multidimensional potential energy surfaces and chemical reaction mechanisms, *Russ. Chem. Rev.* **63**, 883 (1994).
- [50] S. Maeda, Y. Harabuchi, Y. Ono, T. Taketsugu, and K. Morokuma, Intrinsic reaction coordinate: Calculation, bifurcation, and automated search, *Int. J. Quantum Chem.* **115**, 258 (2015).
- [51] P. Caramella, P. Quadrelli, and L. Toma, An unexpected bispericyclic transition structure leading to 4+ 2 and 2+ 4 cycloadducts in the endo dimerization of cyclopentadiene, *J. Am. Chem. Soc.* **124**, 1130 (2002).
- [52] D. H. Ess, S. E. Wheeler, R. G. Iafe, L. Xu, N. Celebi-Oelcuem, and K. N. Houk, Bifurcations on potential energy surfaces of organic reactions, *Angew. Chem. Int. Ed.* **47**, 7592 (2008).
- [53] S. R. Hare and D. J. Tantillo, Post-transition state bifurcations gain momentum—current state of the field, *Pure Appl. Chem.* **89**, 679 (2017).
- [54] J. Rehbein and B. K. Carpenter, Do we fully understand what controls chemical selectivity?, *Phys. Chem. Chem. Phys.* **13**, 20906 (2011).
- [55] J. Rehbein and B. Wulff, Chemistry in motion—off the mep, *Tetrahedron Lett.* **56**, 6931 (2015).
- [56] P. Collins, B. K. Carpenter, G. S. Ezra, and S. Wiggins, Nonstatistical dynamics on potentials exhibiting reaction path bifurcations and valley-ridge inflection points, *J. Chem. Phys.* **139**, 154108 (2013).
- [57] A. Kumar and S. Keshavamurthy, Quantum dynamical studies on a model for reactions exhibiting post-transition state bifurcation, *J. Chem. Sci.* **137**, 114 (2025).
- [58] Z. Tao, T. Qiu, and J. E. Subotnik, Symmetric post-transition state bifurcation reactions with Berry pseudo-magnetic fields, *J. Phys. Chem. Lett.* **14**, 770 (2023).
- [59] Y. Ke, Non-equilibrium origin of cavity-induced resonant modifications of chemical reactivities, *J. Chem. Phys.* **163**, 054109 (2025).
- [60] V. J. García-Garrido and S. Wiggins, The dynamical significance of valley-ridge inflection points, *Chem. Phys. Lett.* **781**, 138970 (2021).
- [61] Z. C. Kramer, B. K. Carpenter, G. S. Ezra, and S. Wiggins, Reaction path bifurcation in an electrocyclic reaction: ring-opening of the cyclopropyl radical, *J. Phys. Chem. A* **119**, 6611 (2015).
- [62] X. Li, A. Mandal, and P. Huo, Cavity frequency-dependent theory for vibrational polariton chemistry, *Nat. Commun.* **12**, 1 (2021).
- [63] J. George and J. Singh, Polaritonic chemistry: Band-selective control of chemical reactions by vibrational strong coupling, *ACS Catal.* **13**, 2631 (2023).
- [64] J. P. Long and B. Simpkins, Coherent coupling between a molecular vibration and fabry–perot optical cavity to give hybridized states in the strong coupling limit, *ACS photonics* **2**, 130 (2015).
- [65] E. W. Fischer, J. Anders, and P. Saalfrank, Cavity-altered thermal isomerization rates and dynamical resonant localization in vibro-polaritonic chemistry, *J. Chem. Phys.* **156**, 154305 (2022).
- [66] J. Sun and O. Vendrell, Suppression and enhancement of thermal chemical rates in a cavity, *J. Phys. Chem. Lett.* **13**, 4441 (2022).
- [67] B. M. Weight, D. J. Weix, Z. J. Tonzetich, T. D. Krauss, and P. Huo, Cavity quantum electrodynamics enables para- and ortho-selective electrophilic bromination of nitrobenzene, *J. Amer. Chem. Soc.* **146**, 16184 (2024).
- [68] S. M. Vega, W. Ying, and P. Huo, Theoretical insights into the resonant suppression effect in vibrational polariton chemistry, *J. Am. Chem. Soc.* **147**, 19727 (2025).
- [69] J. B. Pérez-Sánchez, A. Koner, N. P. Stern, and J. Yuen-Zhou, Simulating molecular polaritons in the collective regime using few-molecule models, *Proc. Natl. Acad. Sci. U.S.A.* **120**, e2219223120 (2023).
- [70] L. P. Lindoy, A. Mandal, and D. R. Reichman, Investigating the collective nature of cavity-modified chemical kinetics under vibrational strong coupling, *Nanophotonics* **13**, 2617 (2024).
- [71] Y. Ke and J. Assan, Harnessing multi-mode optical structure for chemical reactivity, *J. Chem. Phys.* **163**, 164703 (2025).
- [72] E. Mondal, S. M. Vega, and P. Huo, Vibrational strong coupling in cavity qed forms a macroscopic quantum state, *chemrxiv-2025-llc4k* (2025).